STRUCTURAL BIOLOGY

Structural basis for long-chain isoprenoid synthesis by *cis*-prenyltransferases

Moshe Giladi[1,2]*, Michal Lisnyansky Bar-El[1], Pavla Vaňková[3], Alisa Ferofontov[1], Emelia Melvin[1], Suha Alkaderi[1], Daniel Kavan[3], Boris Redko[4], Elvira Haimov[4], Reuven Wiener[5], Petr Man[3], Yoni Haitin[1,6]*

Isoprenoids are synthesized by the prenyltransferase superfamily, which is subdivided according to the product stereoisomerism and length. In short- and medium-chain isoprenoids, product length correlates with active site volume. However, enzymes synthesizing long-chain products and rubber synthases fail to conform to this paradigm, because of an unexpectedly small active site. Here, we focused on the human *cis*-prenyltransferase complex (h*cis*-PT), residing at the endoplasmic reticulum membrane and playing a crucial role in protein glycosylation. Crystallographic investigation of h*cis*-PT along the reaction cycle revealed an outlet for the elongating product. Hydrogen-deuterium exchange mass spectrometry analysis showed that the hydrophobic active site core is flanked by dynamic regions consistent with separate inlet and outlet orifices. Last, using a fluorescence substrate analog, we show that product elongation and membrane association are closely correlated. Together, our results support direct membrane insertion of the elongating isoprenoid during catalysis, uncoupling active site volume from product length.

INTRODUCTION

Isoprenoids are a large group of natural products, abundant across all kingdoms of life (*1*). These compounds are crucial for numerous cellular processes, such as the biosynthesis of cholesterol, steroid hormones, visual pigments, and moieties for posttranslational protein modifications (*2*). Isoprenoids are synthesized by prenyltransferases, a group of enzymes that catalyze the condensation reaction between an allylic diphosphate primer and an isopentenyl diphosphate (IPP, C_5) building block (*3*, *4*). In accordance with the stereoisomerism of the double bond formed during the reaction, these enzymes are subdivided into *cis*- and *trans*-prenyltransferases. Adding further complexity to the system, *cis*-prenyltransferases are also classified into four major classes according to the length of the final product. These classes include short-chain (up to C_{20}), medium-chain (up to C_{60}), long-chain (up to C_{120}), and rubber synthase (>$C_{10,000}$) (*5*, *6*). In addition to the difference in product chain length, *cis*-prenyltransferases differ in their subunit composition. Specifically, while short- and medium-chain producing enzymes are homodimeric, enzymes belonging to the long-chain and rubber synthase classes are heteromeric (*7*).

Despite the huge variance in product chain length and subunit composition, all four *cis*-prenyltransferase classes share an overall conserved structure and catalytic mechanism (*5*, *6*, *8*). The active site is divided into two substrate binding sites termed S_1 and S_2 (Fig. 1A). The allylic diphosphate primer binds at S_1, while IPP binds at S_2. Once both sites are occupied by substrates, with a Mg^{2+} ion serving as an essential cofactor, the diphosphate group of the allylic primer is hydrolyzed, leaving behind a carbocation intermediate that undergoes condensation with IPP. Following the binding of a new IPP molecule at S_2, the cycle can be repeated until a final chain length is reached and the product dissociates. Previously, structure-function studies of short- and medium-chain enzymes suggested that the final chain length is directly related to the volume of S_1 (*9*–*11*). However, the recently determined crystal structures of the long-chain human *cis*-prenyltransferase complex (h*cis*-PT) challenge this view (Fig. 1A) (*12*, *13*). Specifically, the volume of S_1 in the long-chain h*cis*-PT was unexpectedly found to be smaller than that of medium-chain orthologs, making it clearly incompatible with long products. These observations accentuate our missing mechanistic understating of long-chain isoprenoids and rubber synthesis.

h*cis*-PT plays an important role in protein N-glycosylation and thus is ubiquitously expressed in every cell type (*14*). This heteromeric enzyme is composed of two types of subunits: a catalytic subunit termed dehydrodolichyl diphosphate synthase (DHDDS) and an auxiliary quiescent subunit termed Nogo B-receptor (NgBR) (Fig. 1A) (*15*). In line with its important biological roles, mutations in both subunits of h*cis*-PT were identified as causing several human diseases with ocular (*16*, *17*) and neurological (*18*–*21*) manifestations, among others (*22*, *23*). Physiologically, h*cis*-PT is localized to the endoplasmic reticulum (ER) membrane via an N-terminal transmembrane domain of NgBR, where it synthesizes the precursor for dolichol-phosphate (Dol-P) by consecutive condensations of IPP onto the allylic diphosphate primer farnesyl diphosphate (FPP, C_{15}) (Fig. 1B) (*7*, *15*). Dol-P serves as a lipidic glycosyl carrier for N-glycosylation, residing in the ER membrane (*14*, *24*). The structures of the soluble regions of h*cis*-PT (sh*cis*-PT), devoid of the transmembrane region of NgBR (*12*, *13*), revealed that h*cis*-PT is a heterotetramer, formed by two DHDDS-NgBR heterodimers (fig. S1). DHDDS exhibits the common *cis*-prenyltransferase fold, composed of seven α helices (α1 to α7) and six β strands (βA to βF), flanked by an N-terminal helix (αN) and a unique C-terminal helix-turn-helix motif enabling heterotetramerization (fig. S1). Conversely, while NgBR exhibits substantial sequence similarity with *cis*-prenyltransferases, its structure revealed a pseudo–*cis*-prenyltransferase fold, composed of six

[1]Department of Physiology and Pharmacology, Sackler School of Medicine, Tel-Aviv University, Tel-Aviv 6997801, Israel. [2]Tel Aviv Sourasky Medical Center, Tel Aviv 6423906, Israel. [3]Institute of Microbiology of the Czech Academy of Sciences, Division BioCeV, Prumyslova 595, 252 50 Vestec, Czech Republic. [4]Blavatnik Center for Drug Discovery, Tel Aviv University, Tel Aviv 6997801, Israel. [5]Department of Biochemistry and Molecular Biology, IMRIC, Hadassah Medical School, The Hebrew University, Jerusalem 9112001, Israel. [6]Sagol School of Neuroscience, Tel Aviv University, Tel Aviv 6997801, Israel.
*Corresponding author. Email: moshegil@post.tau.ac.il (M.G.); yhaitin@tauex.tau.ac.il (Y.H.)

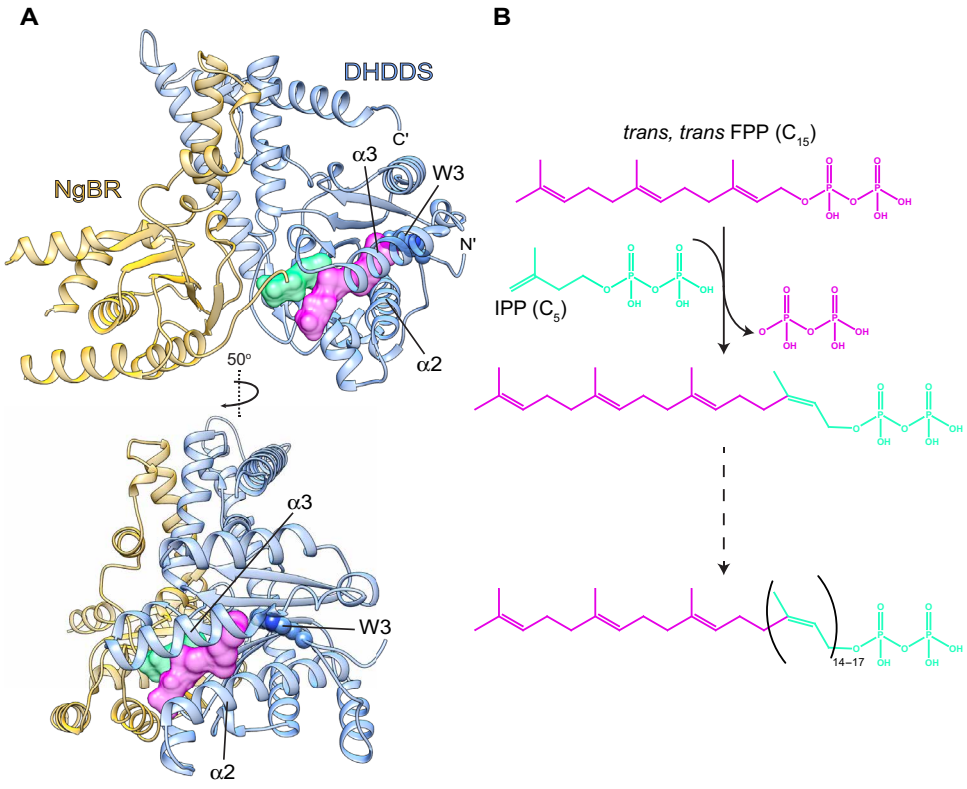

Fig. 1. Overview of h*cis*-PT structure and reaction scheme. (**A**) Cartoon representation of a single DHDDS-NgBR heterodimer in complex with FPP [Protein Data Bank (PDB) 6Z1N] (*12*). DHDDS and NgBR are colored blue and yellow, respectively. Surface representations of the FPP and IPP [placed by superposition with PDB 6W2L (*13*)] molecules are colored pink and green, respectively. The residue W3, at the DHDDS N terminus, is shown as spheres. (**B**) Condensation reaction scheme. At the first cycle, the allylic diphosphate primer, FPP (C_{15}, pink), undergoes a condensation with IPP (C_5, green) to produce geranylgeranyl-diphosphate (GGPP) (C_{20}). The cycle repeats with further condensations (14–17) of the allylic diphosphate at S_1, ultimately leading to a final product length of $C_{85–100}$.

α helices (α1 to α6) and five β strands (βA to βE) (fig. S1) (*25*). Although NgBR has no endogenous *cis*-prenyltransferase activity, it accelerates that activity of DHDDS ~400-fold by direct interaction of the NgBR C-terminal tail with active site residues and substrates (*12*, *26*).

In all *cis*-prenyltransferases, the hydrophobic pocket of S_1 is surrounded by two α helices (α2 and α3) and four β strands (βA, βB, βE, and βF). However, the structural elements forming the active site "bottom", juxtaposing the pyrophosphate binding region (Fig. 1A), differ between the different classes. In short- and medium-chain enzymes, the bottom consists of rigidly and tightly packed bulky hydrophobic residues, leaving the active site inlet as the only orifice to the bulk solvent. Mutations of these bulky residues at the bottom of the active site change the available volume for product elongation, altering product length (*27*). In contrast, long-chain enzymes harbor a unique N-terminal tail forming the active site bottom. Specifically, an insertion in α3 leads to active site widening, allowing the N-terminal tail of DHDDS to snake into the active site, with the conserved residue W3 strategically situated as a stopcock preventing exposure of the hydrophobic pocket to the bulk solution (Fig. 1A) by forming hydrophobic interactions with F55 (α2), F101 (α3), and V152 (βD).

Here, to elucidate the structural basis for long-chain isoprenoid synthesis by h*cis*-PT, we combined x-ray crystallography, hydrogen-deuterium exchange mass spectrometry (HDX-MS), fluorescence spectroscopy, as well as biochemical and functional analyses. By determining multiple crystal structures of sh*cis*-PT in the presence of reactive and nonreactive substrate analogs, we halted catalysis and captured the enzyme in specific predefined states along its catalytic cycle. Notably, following a single condensation reaction, the N terminus of DHDDS translocates, resulting in opening of a novel outlet through which the C_{20} product extends toward the bulk solvent, as supported by limited proteolysis analysis. In line with the crystal structures, HDX-MS studies of apo sh*cis*-PT reveal that the N terminus of DHDDS is highly dynamic in solution, supporting the propensity of the novel outlet to form. Moreover, we show using functional assays that side chain hydrophobicity at position 3 is crucial for enzymatic function and that W3 dictates the rate of the first condensation. Last, fluorescence resonance energy transfer (FRET) measurements between a fluorescent FPP analog and fluorescently labeled lipid nanodiscs indicate direct product elongation into the lipid bilayer. Together, our results depict a product elongation mechanism involving its dynamic interplay with the N-terminal tail of DHDDS, where expulsion of W3 results in the formation of an outlet through which product immersion into the adjacent lipid bilayer can be achieved, circumventing the need for housing long-chain products. Moreover, this mechanism may also explain the activity enhancement of h*cis*-PT observed in the presence of detergents or lipids (*13*, *28*), as well as the molecular basis for natural rubber synthesis (*6*).

RESULTS

sh*cis*-PT crystallization with nonreactive substrates exposes discrete states along the first condensation reaction

Previously, the catalytic mechanism facilitating the condensation reaction by *cis*-prenyltransferases was extensively studied, with residues involved in the reaction mechanism shown to be highly conserved among the different classes (*5*–*8*, *10*). However, the molecular mechanism enabling the accommodation of long-chain products remains to be resolved. Hence, to dissect the conformational states along the condensation reaction, we analyzed the conformational transitions associated with the first catalytic cycle using reactive and nonreactive substrate analogs (Fig. 2 and Table 1). To this end, we purified sh*cis*-PT_{cryst}, consisting of full-length DHDDS (residues 1 to 333) and the pseudo *cis*-prenyltransferase domain of NgBR (residues 73 to 293) lacking residues 167 to 175, followed by crystallization and structure determination in the presence of different substrates combinations. As sh*cis*-PT produces product population ranging in lengths (Fig. 1B), this approach favors the formation of specific and highly homogeneous enzyme-substrate complexes, facilitating our structural investigations. In all four structures determined here, the asymmetric unit of the crystal consists of a single heterodimer. The heterotetramer is formed via a dimerization interface between adjacent asymmetric units, mainly consisting of the C terminus of DHDDS (fig. S1).

To isolate the initial substrate-bound state, where FPP and IPP occupy S_1 and S_2, respectively, we crystallized sh*cis*-PT_{cryst} in the presence of Mg^{2+}, farnesyl thiodiphosphate (FsPP) and IPP (*29*, *30*). The replacement of the hydrolysable oxygen with a sulfur atom in FsPP results in a poorly reactive substrate compared with FPP (Fig. 2A), allowing us to capture the precondensation state. Next, to resolve the enzyme harboring the product of the first condensation reaction, we crystallized the complex in the presence of Mg^{2+}, FPP, and isopentenyl thiodiphosphate (IsPP) (Fig. 2B) (*30*). The condensation of FPP with IsPP results in the formation of geranylgeranyl thiodiphosphate (GGsPP), which is recalcitrant for further condensations, due to the same mechanism as in the case of FsPP. Serendipitously, we were able to obtain two different forms of this GGsPP-bound enzyme, one containing a sulfate ion (Fig. 2B) and the other IsPP (Fig. 2C), bound at S_2. Last, we crystallized sh*cis*-PT_{cryst} in the presence of geranylgeranyl-diphosphate (GGPP) and IsPP as initial substrates (Fig. 2D), with the goal of obtaining a structure corresponding to sh*cis*-PT_{cryst} in complex with the second condensation product farnesylgeranyl diphosphate (C_{25}). However, the protein only crystallized in the precondensation state, with the substrates GGPP and IsPP bound at S_1 and S_2, respectively.

NgBR-R290 changes its conformation along the catalytic cycle

Previously, the structure of sh*cis*-PT_{cryst} was determined in the presence of FPP at S_1 and a phosphate group at S_2 (*12*) or in a state where IPP occupies both sites (*13*). In contrast, the structures reported here represent native states in which both sites are occupied by their respective substrates. Thus, we first focused on the organization of the superficial polar region, involved in pyrophosphate binding, along the reaction cycle (Fig. 2). At S_1, the pyrophosphate group of FsPP (Fig. 2A), GGsPP (Fig. 2, B and C), or GGPP (Fig. 2D) interacts with a Mg^{2+} ion and is also stabilized by interactions with R37, R38, and R85 from DHDDS. At S_2, the pyrophosphate group of IPP (Fig. 2A), the sulfate ion (Fig. 2B), or the pyrophosphate of IsPP (Fig. 2, C and D) is stabilized by R205, R211, and S213 from DHDDS and the backbone nitrogen of G292 from NgBR. In all the structures, the NgBR C-terminal carboxylate (K293) interacts with R37 and R85 of DHDDS, involved in substrate coordination at S_1 (Fig. 2).

The structure with bound FsPP and IPP (Fig. 2A) reveals that the simultaneous occupancy of S_1 and S_2 does not alter the conformation of the substrates, compared with structures obtained in complex with either substrate alone (fig. S2). However, the presence of IPP (Fig. 2A) or IsPP (Fig. 2, C and D), rather than sulfate (Fig. 2B) or phosphate (*12*), at S_2 results in two main changes. First, the orientation of R290 from NgBR is altered (Fig. 2, A, C, and D versus Fig. 2B). Specifically, while R290 does not interact with the sulfate moiety, it directly interacts with D34 and the substrates in the IPP or IsPP bound states. Intriguingly, underscoring the potential importance of these interactions for catalysis, the R290H mutation reduces catalytic activity in vitro and results in a congenital glycosylation disorder (*12*, *22*, *28*). Second, while Mg^{2+} is octahedrally coordinated via six oxygen atoms, contributed by the conserved D34, the pyrophosphate of FPP, and water molecules in all the structures, one water molecule is replaced by an oxygen from the pyrophosphate group of IPP or IsPP (Fig. 2, A, C, and D). Previously, it was proposed that after FPP binding to S_1, a preformed Mg^{2+}-IPP complex binds to S_2, followed by translocation of the Mg^{2+} ion closer to S_1, enabling the facilitation of pyrophosphate hydrolysis (*5*). Thus, the structures containing an allylic diphosphate at S_1 and IPP or IsPP at S_2, in which the Mg^{2+} ion is coordinated by the pyrophosphate moieties from both sites, likely represent an intermediate in Mg^{2+} translocation.

The N terminus of DHDDS displays conformational plasticity along the catalytic cycle

Previous crystallographic investigations of sh*cis*-PT_{cryst} revealed that the N terminus of DHDDS snakes into the active site, blocking a potential outlet for the elongating product (Fig. 1A) (*12*, *13*). In the presence of FsPP and IPP (Fig. 3A), the conformations of the farnesyl (C_{15}) moiety and the N terminus of DHDDS are similar to those previously observed in the FPP-bound state (Fig. 1A and fig. S2). Unexpectedly, the structures harboring GGsPP or GGPP, following the first condensation reaction (Fig. 2, B to D), demonstrate distinct conformations of the geranylgeranyl (C_{20}) moiety and the N terminus of DHDDS (Fig. 3, B to D). Specifically, unlike the structure with FPP, both GGsPP-bound structures show bending of the geranylgeranyl moiety at C_{11}, resulting from interaction of the terminal carbon (C_{20}) with F154 (βD) within the hydrophobic pocket (Fig. 3, B and C). Comparison of the two GGsPP-bound structures reveals that the N terminus of DHDDS (up to G7) is only resolved in the absence of IsPP (Fig. 3, E and F), pointing toward the dynamic nature and consistent with the high B-factors of this region. Thus, the GGsPP-IsPP bound form reveals a conformation in which the hydrophobic pocket is vacant of W3 and exposed to the bulk solvent. This conformation represents a state in which the enzyme is predisposed for product expulsion and subsequent elongation. In accordance, the GGPP-bound structure notably revealed an elongated conformation, where the terminal carbons are expulsed from the hydrophobic pocket and are exposed to the bulk solvent (Fig. 3, D to F).

To further demonstrate the interplay between the chain length at S_1 and the N-terminal dynamics, we performed limited proteolysis analysis of sh*cis*-PT in the apo-, FPP-bound, and GGPP-bound states (Fig. 3G). Digestion with trypsin, chymotrypsin, or elastase resulted in the cleavage of a ~3-kDa peptide from DHDDS in the apo state. Incubation with FPP completely protected DHDDS from this proteolytic cleavage, while incubation with GGPP resulted in digestion

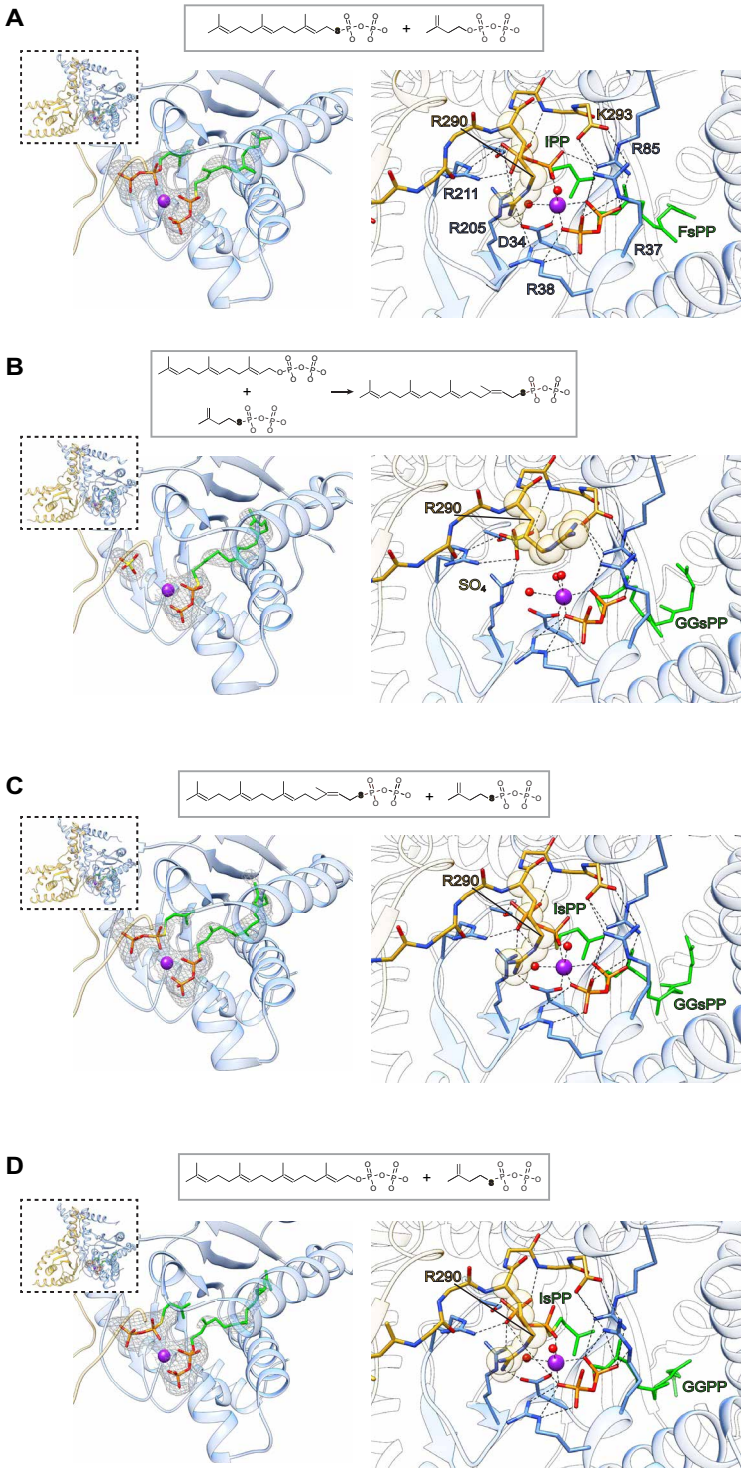

Fig. 2. Structural analysis of sh*cis*-PT$_{cryst}$ reveals active site reorganization along the first condensation cycle. (**A** to **D**) Cartoon representation of a single DHDDS-NgBR heterodimer (left column) and zoomed-in perspectives of the S_1 and S_2 inlet (right column) in complex with FsPP and IPP (A), GGsPP and sulfate (B), GGsPP and IsPP (C), or GGPP and IsPP (D). DHDDS and NgBR are colored blue and yellow, respectively. Coordinating residues, bound substrates, and/or products are shown as sticks. Mg^{2+} and water molecules are shown as purple and red spheres, respectively. A difference map ($DF_o - mF_c$) is shown as a gray mesh (contoured at $\sigma = 2.5$). Polar interactions are highlighted as dashed black lines, and R290 is highlighted by spheres.

Table 1. Data collection and refinement statistics. Note: Statistics are based on one crystal per dataset. Values in parentheses are for the highest-resolution shell. RMS deviations, root mean square deviations.

	sh*cis*-PT$_{cryst}$-FsPP-IPP (PDB 7PAX)	sh*cis*-PT$_{cryst}$-GGsPP (PDB 7PAY)	sh*cis*-PT$_{cryst}$-GGsPP-IsPP (PDB 7 PB0)	sh*cis*-PT$_{cryst}$-GGPP-IsPP (PDB 7 PB1)
Data collection				
Space group	*R*32:*H*	*R*32:*H*	*R*32:*H*	*R*32:*H*
Cell dimensions				
***a*, *b*, *c* (Å)**	184.0, 184.0, 112.5	184.4, 184.4, 112.4	184.1, 184.1, 113.1	183.5, 183.5, 112.3
α, β, γ (°)	90, 90, 120	90, 90, 120	90, 90, 120	90, 90, 120
Resolution (Å)	46.00–2.00(2.12–2.00)	46.10–2.40(2.55–2.40)	46.20–2.30(2.44–2.30)	45.86–2.57(2.64–2.57)
R_{meas}	0.066(1.965)	0.116(0.983)	0.140(1.112)	0.200(2.598)
$CC_{1/2}$ (%)	100(73.1)	99.5(50.4)	99.5(54.7)	99.5(13.9)
$I / \sigma I$	24.4(1.3)	6.8(1.1)	8.2(1.4)	8.6(1.1)
Completeness (%)	96.3(100.0)	99.3(99.1)	99.3(96.9)	89.7 (57.8)
Redundancy	20.9(21.4)	2.9(2.9)	4.4(4.2)	6.0(3.0)
Refinement				
Resolution (Å)	41.12–2.00	46.11–2.40	46.21–2.30	45.87–2.59
No. of reflections	47370	28655	32736	20634
R_{work} / R_{free}	0.2047/0.2325	0.2026/0.2447	0.1939/0.2367	0.2052/0.2490
No. of atoms				
Protein	4075	3991	3942	3653
Ligand/ion	39	35	44	44
Water	79	80	130	2
***B*-factors**	67.9	68.7	52.6	82.7
Protein	68.1	69.0	52.6	82.9
Ligand/ion	60.0	64.4	56.0	73.7
Water	58.8	56.3	51.1	53.6
RMS deviations				
Bond lengths (Å)	0.004	0.005	0.005	0.004
Bond angles (°)	0.77	1.04	1.06	0.68
Ramachandran favored (%)	98.1	97.1	96.9	96.0
Ramachandran allowed (%)	1.9	2.9	3.1	4.0
Ramachandran outliers (%)	0	0	0	0

pattern reminiscent of the apo state. This is in agreement with the crystallographic data, suggesting that in the presence of FPP, the DHDDS N terminus is compactly packed and stabilized by the interaction of W3 with the substrate (Fig. 3A), while in the presence of GGPP, the N terminus exhibits higher lability (Fig. 3D).

Conservation analysis of DHDDS revealed that W3 is highly conserved (*12*). Our crystallographic and limited proteolysis analyses suggest that the tryptophan side chain is strategically positioned, forming an effective barrier between the hydrophobic pocket and the bulk solvent. Thus, we sought to determine whether the hydrophobicity of the side chain at this position is essential. To this end, we systematically replaced W3 with A, L, F, R, or Q (Fig. 3H) and tested their ability to complement a previously described triple-deletion yeast strain lacking the endogenous yeast *cis*-PT subunits (*22*). While the A, L, and F substitutions were able to complement the yeast and induce growth similar to the wild type (WT), the positively charged W3R completely failed to rescue the phenotype, and the hydrophilic W3Q demonstrated slightly diminished complementation capacity. Collectively, the structures of sh*cis*-PT$_{cryst}$ along the reaction cycle, supported by biochemical and functional analyses, reveal that both the product and the DHDDS N terminus are inherently flexible, allowing the formation of a novel outlet for streamlined synthesis of long-chain products.

HDX-MS analysis reveals that the N terminus of DHDDS is highly dynamic in solution

To determine the conformational dynamics of the N terminus, governing the formation propensity of the novel hydrophobic pocket

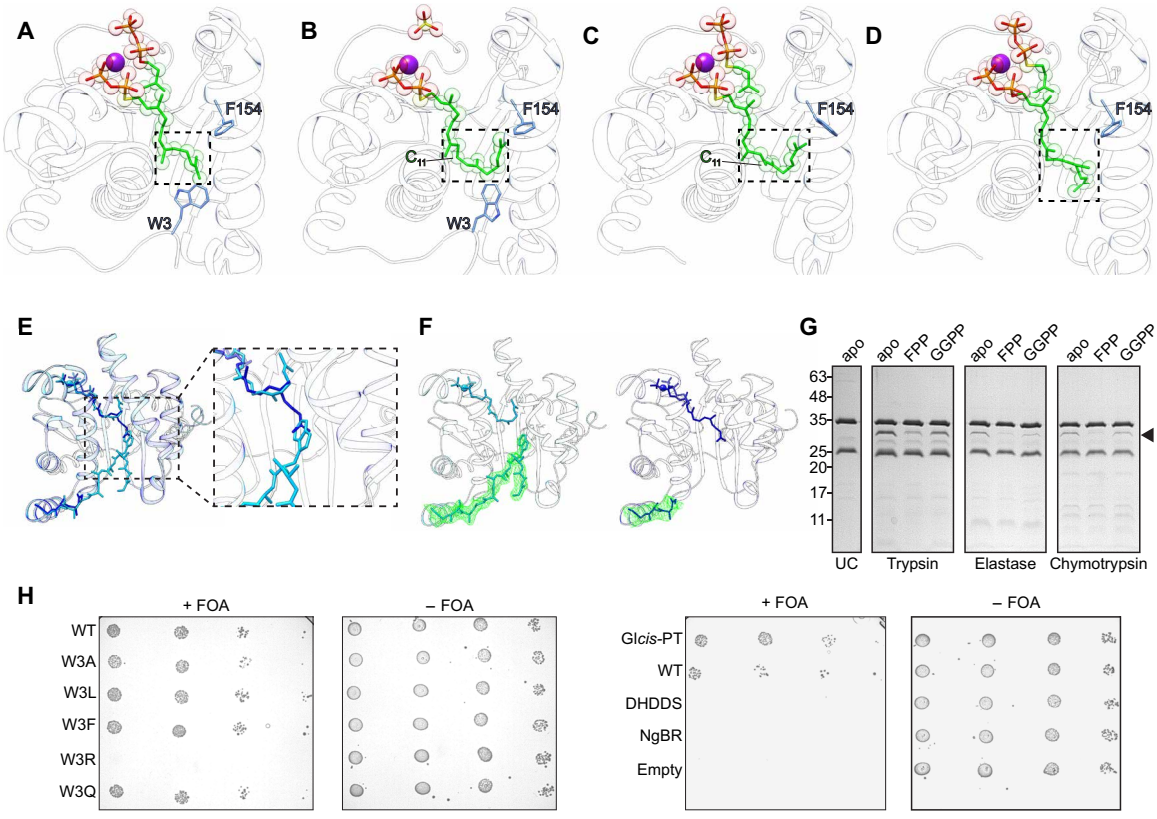

Fig. 3. The N terminus of DHDDS translocates from the active site outlet during the catalytic cycle. (**A** to **D**) Cartoon representations of DHDDS in complex with FsPP and IPP (A), GGsPP and sulfate (B), GGsPP and IsPP (C), and GGPP and IsPP (D). Bound substrates, W3, serving as a stopcock for the active site outlet, and F154, stabilizing the bent conformation of the C_{20} product within the active site, are shown as sticks. The terminal carbons of the substrate at S_1 are framed. (**E**) Superposition of sh*cis*-PT_{cryst} in complex with GGsPP (cyan) and GGPP-IsPP (blue). The N terminus of DHDDS, GGsPP, and GGPP are shown as sticks. (**F**) $2F_o - F_c$ electron density maps of the N terminus of DHDDS, contoured at σ = 1, are shown as green mesh for sh*cis*-PT_{cryst} in complex with GGsPP (left) and GGPP-IsPP (right). No electron density could be identified upstream of residue G7. (**G**) SDS–polyacrylamide gel electrophoresis (SDS-PAGE) analysis of sh*cis*-PT following limited proteolysis by the indicated proteases, in the presence or absence of substrates, as described in Materials and Methods. The DHDDS cleavage product is indicated by an arrow. (**H**) KG405 cells were cotransformed with h*cis*-PT harboring the indicated DHDDS subunits. Transformants were plated in serial dilutions with or without 5-fluoroorotic acid (FOA), as indicated (left). W3R failed to produce functional complementation. Gl*cis*-PT served as a positive control, and transformations with either subunit (DHDDS or NgBR) or empty vectors were used as negative controls (right). WT, wild type.

outlet, we performed HDX-MS analysis of apo sh*cis*-PT. In this method, the protein sample is diluted in deuterated buffer solution, resulting in the exchange of hydrogens with deuterium (*31*, *32*). The reaction is quenched at different time points, followed by proteolytic digestion and quantitation of deuterium incorporation on backbone amides within each peptide (*32*). The exchange rate reflects the local fold and solvent accessibility of each protein region. Following proteolytic digestion, we were able to obtain a 100 and 98.7% coverage for DHDDS and NgBR, respectively (fig. S3).

Overall, sh*cis*-PT exhibited a characteristic HDX pattern for a soluble protein, where the core, secondary structure elements and buried interfacial regions show low HDX (Fig. 4A). Focusing on the active site, the HDX profile revealed three distinct regions displaying alternating HDX levels (Fig. 4). First, the inlet (Fig. 4A), composed of α1, the N-terminal portions of α2 and α3, and the C-terminal tail of NgBR (Fig. 4B), exhibited relatively high HDX. This is consistent with previous studies of medium-chain orthologs, suggesting local unfolding of the pyrophosphate binding region in the absence of substrates. Second, the hydrophobic pocket (Fig. 4A), which includes the C-terminal portion of α2, the middle of α3, βA, βB, and the C-terminal portion of βC and βD (Fig. 4B), exhibited the lowest HDX as expected from a rigid, well-structured, and solvent-inaccessible segment. Last, the outlet (Fig. 4A), composed of the C-terminal portion of α3, the N-terminal portion of βC, and the N terminus of DHDDS (residues 2 to 11) (Fig. 4B), displayed higher HDX compared to the hydrophobic core. The dynamics of the C-terminal portion of α3 are in agreement with its previously suggested role in active site widening and accommodation of long-chain products during catalysis. Moreover, the N terminus of DHDDS exhibited notably high HDX throughout the experiment (Fig. 4B), indicating that it is highly labile in solution. Together, the alternating pattern of solvent exposure within the active site supports directional product processing, with an inlet at the pyrophosphate binding region and an outlet at the distal hydrophobic pocket.

A fluorescent FPP analog as a tool for structure-function investigations of sh*cis*-PT

Long-chain *cis*-prenyltransferases and rubber synthases are membrane delimited, and the presence of detergents or phospholipids was shown to markedly enhance their catalytic activity (*6*, *13*, *28*). As our structural studies suggest product elongation through a novel

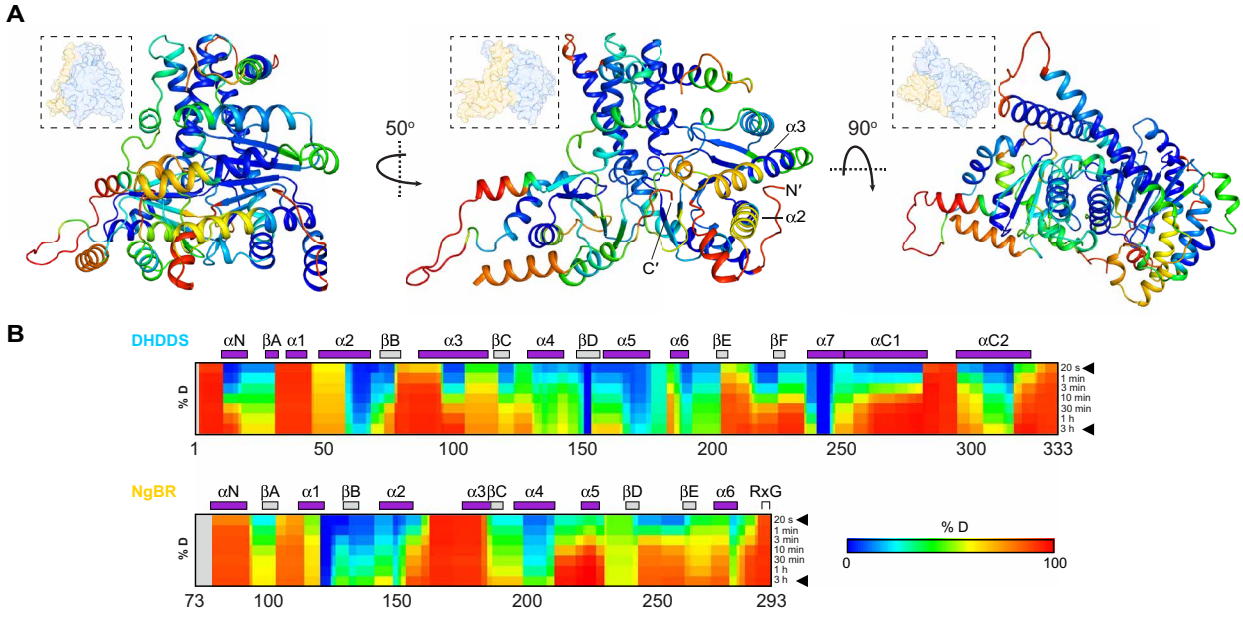

Fig. 4. HDX-MS profile of sh*cis*-PT active site supports separated and dynamic inlet and outlet. (**A**) Cartoon representations of a single DHDDS-NgBR heterodimer. Heatmap coloring represents the HDX level following 20-s incubation in D_2O, with highest and lowest exchange levels indicated in red and blue, respectively. In each orientation, an inset provides a DHDDS (blue) and NgBR (yellow) heterodimer surface representation, for orientation purpose. The N terminus, α2, and α3 of DHDDS and the C terminus of NgBR are indicated. (**B**) Deuteration levels at the indicated time points for DHDDS (top) and NgBR (bottom). The secondary structures elements are indicated above the heatmaps for each protein.

outlet, possibly into the adjacent membrane, we sought to monitor the chemical environment and position of the elongating isoprene moiety. To this end, we used the fluorescent FPP analog (2*E*,6*E*)-8-*O*-(*N*-methyl-2-aminobenzoyl)-3,7-dimethyl-2,6-octandien-1-pyrophosphate (MANT-O-GPP) (*33*), which was previously used to measure the activity of medium-chain enzymes.

To validate that MANT-O-GPP is a bona fide substrate for sh*cis*-PT, we used a radioactivity-based enzyme kinetics assay (Fig. 5A), revealing that MANT-O-GPP exhibits Michaelis constant (K_m) = 0.14 ± 0.01 μM (n = 3), similar to that previously reported for FPP (*12*). Next, as the excitation profile of MANT-O-GPP closely resembles the emission profile of tryptophan (Fig. 5B), we reasoned that FRET can be used to assess the binding and position of MANT-O-GPP at S_1. Specifically, the fluorescent MANT moiety is expected to reside in subnanometer proximity with W3 (Fig. 5C), within FRET distance (*34*). By using tryptophan excitation (F_{280}) in the presence of increasing [MANT-O-GPP], we observed an increase in FRET. This is reflected by the concomitant decrease in tryptophan (F_{340}) and increase in MANT-O-GPP (F_{420}) emissions (Fig. 5D). Notably, no direct MANT-O-GPP fluorescence is observed by excitation with F_{280} in the absence of sh*cis*-PT (Fig. 5D). Moreover, following incubation with constant [MANT-O-GPP] (10 μM) and increasing [FPP], we observed an FPP-dependent FRET reduction [IC_{50} (half-maximal inhibitory concentration) = 10.5 ± 3.0 μM, n = 3] (Fig. 5E). This is reflected by an increase in F_{340} and a reciprocal decrease in F_{420}, indicating that MANT-O-GPP and FPP share a common site. Last, as DHDDS and NgBR contain eight and three tryptophan residues, respectively, each possibly contributing to the FRET signal, we sought to dissect the relative contribution of W3. Therefore, we purified the W3L mutant, supporting yeast complementation (Fig. 3H) and maintaining the hydrophobicity of this position while abolishing its fluorescence (Fig. 5F). While the WT and W3L mutant exhibit MANT-O-GPP–dependent FRET (Fig. 5F), with a nearly identical dissociation constant for MANT-O-GPP (1.06 ± 0.04 μM versus 0.94 ± 0.09 μM, P = 0.33, n = 3), the lack of tryptophan at position 3 results in a significant reduction in the F_{420}/F_{340} ratio (2.99 ± 0.04 versus 1.77 ± 0.05, $P < 0.0001$, n = 3) (Fig. 5G). Thus, MANT-O-GPP resides in close proximity to W3, as FPP, at the outlet of S_1.

The structure of sh*cis*-PT in complex with GGPP (Figs. 2D and 3D) suggests that W3 is displaced during the first condensation reaction. Thus, we explored the effect of W3L on chain elongation by sh*cis*-PT. Enzyme kinetics analysis revealed similar K_m (0.1 ± 0.008 and 0.04 ± 0.005 μM, respectively) and turnover number (k_{cat}) values (0.74 ± 0.01 and 0.69 ± 0.02 s^{-1}) for WT and W3L, respectively (Fig. 6A). However, these measurements reflect the formation of long-chain products emanating from consecutive condensation reactions. To focus on the first condensation, during which the displacement of W3 should take place, we resorted to the use of the nonreactive substrate IsPP to limit the reaction to a single condensation, as described above. Stopped-flow kinetics measurements revealed that the first condensation by W3L is significantly faster compared with the WT (Fig. 6B). Specifically, while sh*cis*-PT WT displayed observed rate constant (k_{obs}) = 3.1 ± 0.2 s^{-1}, sh*cis*-PT W3L displayed k_{obs} = 4.3 ± 0.2 s^{-1} (Fig. 6C). This is consistent with a lower energetic barrier for the displacement of the less bulky leucine from the hydrophobic pocket compared with the native tryptophan.

sh*cis*-PT catalytic activity correlates with product-membrane interaction

To determine whether the membrane bilayer can interact with and possibly house the elongating product, we first assessed the effect of azolectin nanodiscs on the catalytic activity of sh*cis*-PT. These measurements rely on the increased inherent MANT-O-GPP emission at F_{420} upon chain elongation (*33*). Consistent with the ability of

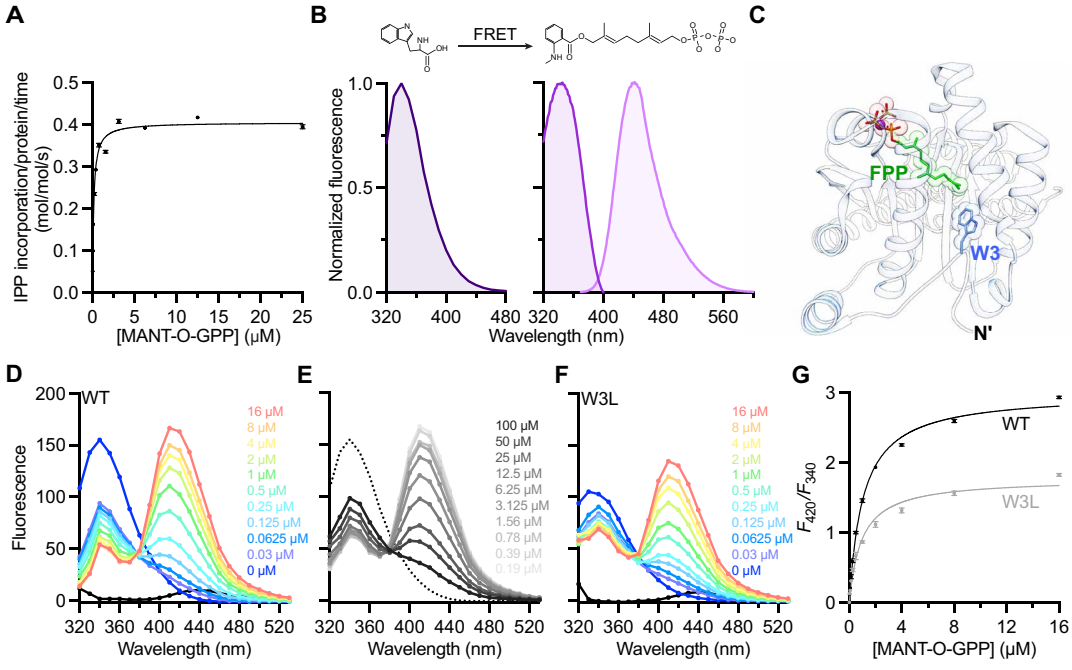

Fig. 5. MANT-O-GPP binds at S_1 and is a viable substrate of sh*cis*-PT. (**A**) MANT-O-GPP–dependent sh*cis*-PT activity in the presence of 100 μM IPP, measured as ^{14}C-IPP incorporation ($n = 3$, mean ± SEM). (**B**) Tryptophan emission spectrum (left) and MANT-O-GPP excitation (purple) and emission (pink) spectra (right). The chemical schemes of tryptophan and MANT-O-GPP are depicted. (**C**) Cartoon representation of sh*cis*-PT$_{cryst}$ in complex with FPP (PDB 6Z1N), highlighting the close proximity between FPP (green sticks) and W3 (blue sticks). (**D** to **F**) Average fluorescence emission spectra following excitation at F_{280}. Increasing concentrations of MANT-O-GPP resulted in concomitant decrease of F_{340} and increase of F_{420} in sh*cis*-PT–WT ($n = 3$) (**D**) or W3L mutant ($n = 3$) (**F**). Increasing FPP concentrations, in the presence of constant MANT-O-GPP (10 μM) resulted in concomitant increase of F_{340} and decrease of F_{420}, indicating MANT-O-GPP displacement ($n = 3$) (**E**). (**G**) F_{420}/F_{340} as a function of MANT-O-GPP concentration, measured using sh*cis*-PT–WT or W3L ($n = 3$, mean ± SEM).

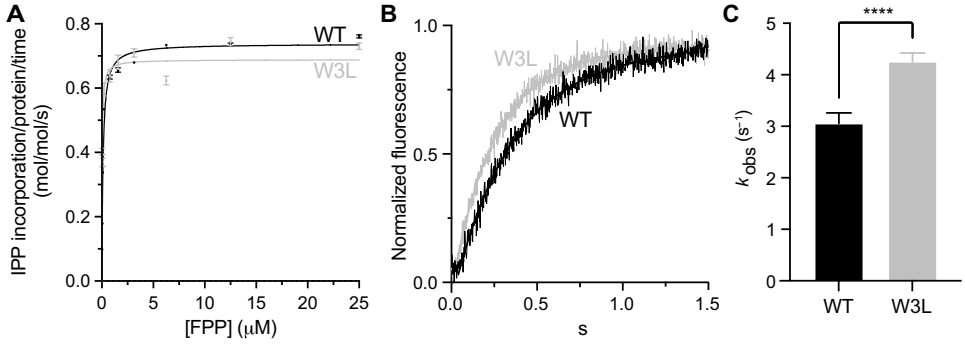

Fig. 6. W3 is involved in determining the rate of the first condensation by sh*cis*-PT. (**A**) FPP-dependent activity was measured as ^{14}C-IPP incorporation in the presence of 100 μM IPP. Data are presented as means ± SEM, $n = 3$. (**B**) Averaged stopped-flow kinetics of a single condensation reaction measured using FRET as described in Materials and Methods. sh*cis*-PT (2 μM; WT or W3L) preincubated with 2 μM MANT-O-GPP was mixed in a 1:1 ratio with 10 μM IsPP. Data were fit to a single-exponential equation. (**C**) Rate constants determined from individual stopped-flow kinetics traces presented as means ± SEM ($n = 14$ and 20 for WT and W3L, respectively; unpaired *t* test with Welch's correction; ****$P < 0.0001$).

phospholipids to enhance sh*cis*-PT activity (*13*), inclusion of nanodiscs at increasing nanodisc/enzyme ratios resulted in increased fluorescence amplitude and slope over the reaction time course (Fig. 7A). Next, to examine the interplay between the membrane and product length, we used thin-layer chromatography (TLC) analysis with MANT-O-GPP as a substrate (Fig. 7B). Consistent with the fluorescence intensity measurements (Fig. 7A), the TLC analysis revealed that incubation with nanodiscs enhanced product formation (Fig. 7B). Moreover, products distribution was shifted toward longer lengths in the presence of nanodiscs. Next, we measured FRET between MANT-O-GPP, serving as a donor, and azolectin nanodiscs containing 1% (mol/mol) 1,2-dioleoyl-*sn*-glycero-3-phosphoethanolamine-*N*-(7-nitro-2-1,3-benzoxadiazol-4-*yl*) (PE-NBD), a fluorescently labeled phospholipid, serving as an acceptor (Fig. 7, C and D). Following incubation of sh*cis*-PT with MANT-O-GPP, IPP, and the fluorescent nanodiscs, we measured the fluorescence spectrum resulting from excitation of MANT-O-GPP (F_{352}) (Fig. 7D). In the absence of active catalysis (e.g., in the presence

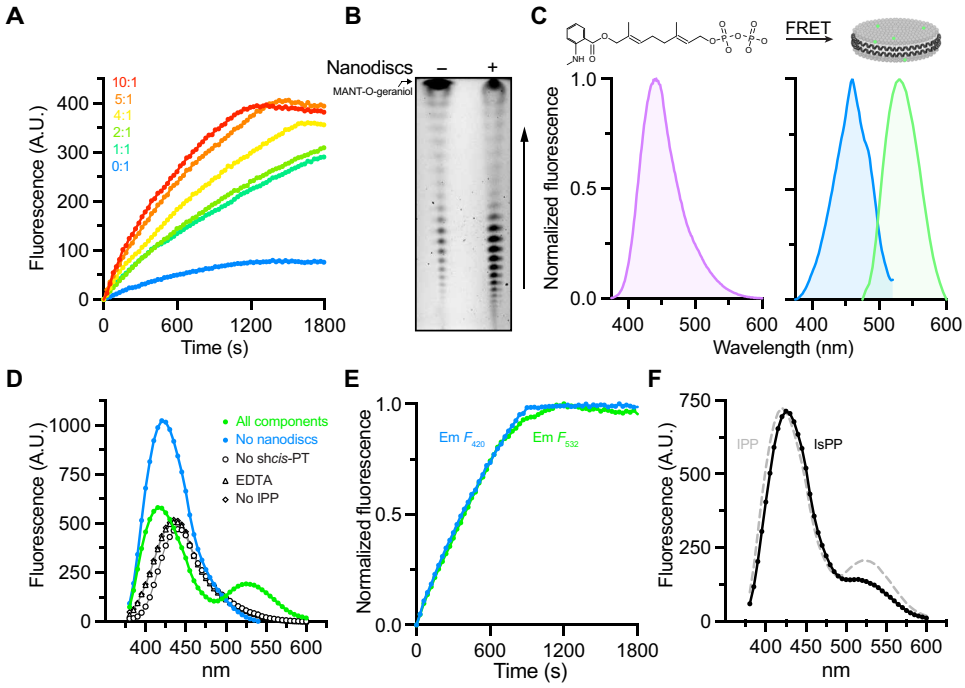

Fig. 7. Direct product-lipid interactions enhance long-chain isoprenoid synthesis by sh*cis*-PT. (**A**) Average time-dependent increase in MANT-O-GPP fluorescence (F_{420}) in the presence of increasing MSP1D1E3 nanodisc molar ratios ($n = 3$ for each molar ratio). A.U., arbitrary units. (**B**) TLC analysis of the reaction products formed in the absence (–) or presence (+) of nanodiscs (2:1 nanodiscs:sh*cis*-PT ratio), with MANT-O-GPP as a substrate, detected using ultraviolet illumination ($\lambda = 365$ nm). (**C**) MANT-O-GPP emission spectrum (left) and PE-NBD excitation (blue) and emission (green) spectra (right). The experimental scheme is depicted above spectra. (**D**) Averaged fluorescence emission spectra following excitation at F_{352}. Incubation of sh*cis*-PT in the presence of MANT-O-GPP, IPP, Mg^{2+}, and PE-NBD–labeled nanodiscs ("all components") resulted in a fluorescence peak corresponding to PE-NBD emission (F_{532}) due to FRET (green) ($n = 3$ for each condition). No FRET was observed upon omitting any of the reaction constituents. (**E**) Average time-dependent MANT-O-GPP fluorescence (F_{420}) and PE-NBD FRET (F_{532}) traces reveal nearly identical time dependence ($n = 3$). Em, emission. (**F**) Comparison of the averaged fluorescence emission spectra following excitation at F_{352} and incubation of sh*cis*-PT in the presence of "all components" with IsPP instead of IPP (black) ($n = 3$). The emission spectra in the presence of IPP is shown as dashed gray curve.

of EDTA or the absence of sh*cis*-PT or IPP), no fluorescence peak corresponding to PE-NBD emission is observed. However, inclusion of all components required for catalysis resulted in FRET between MANT-O-GPP and PE-NBD, as reflected by the emergence of a fluorescence peak at F_{532}. These results indicate that chain elongation is a prerequisite for the FRET between the MANT and NBD moieties. Time-dependent measurements of the inherent MANT-O-GPP fluorescence and the MANT-NBD FRET were nearly identical (Fig. 7E). To determine the minimal length required for product-membrane interaction, we limited the reaction to a single condensation and monitored the FRET signal following incubation of sh*cis*-PT with MANT-O-GPP, fluorescent nanodiscs, and IsPP in lieu of IPP (Fig. 7F). This measurement revealed that even a single condensation is sufficient to give rise to FRET between the MANT and NBD moieties although diminished. Together, these results support the notion that during long-chain isoprenoid synthesis by h*cis*-PT, product elongation and its membrane interaction are interlaced.

DISCUSSION

Members of the *cis*-prenyltransferase family show a high level of sequence conservation, translating into highly similar three-dimensional structures (*5*, *7*, *10*). Although sharing an identical catalytic mechanism, the final product length drastically varies between different *cis*-prenyltransferase subclasses (*5*, *6*). While in short- and medium-chain enzymes the product length correlates with active site volume (*9*–*11*), recent structural analyses of the long-chain h*cis*-PT revealed that its active site is seemingly incompatible with such product lengths (Fig. 1) (*12*, *13*). The mismatch between the active site volume and product size is expected to aggravate in rubber synthases, producing extremely long (>$C_{10,000}$) isoprenoids (*6*). Thus, products generated by the long-chain and rubber synthase subclasses were hypothesized to elongate directly into neighboring cellular membranes, obviating the need for a large active site and implying a directional product expulsion via a previously unknown outlet during catalysis (*6*, *12*). Here, we used a hybrid approach to resolve the structural basis and determine the mechanism for long-chain isoprenoid synthesis.

Previously determined structures of sh*cis*-PT in complex with either FPP or IPP revealed that the hydrophobic pocket of DHDDS is occluded from the hydrophilic environment by the conserved W3, situated at the N terminus of DHDDS (Fig. 1A) (*12*, *13*). The importance of a hydrophobic side chain at this position is supported by the yeast complementation analysis (Fig. 3H). The close proximity between FPP and W3 suggested that chain elongation should lead to translocation of the DHDDS N terminus, thereby opening an alternative outlet through which the product can directly and directionally be expulsed. Thus, we crystallized sh*cis*-PT_{cryst} in the presence of different reactive and nonreactive substrates with a goal to capture the enzyme at different points along its catalytic cycle (Fig. 2). The structures revealed that the active site experiences

conformational plasticity along the catalytic cycle to enable long-chain isoprenoid synthesis.

Analysis of the different states captured (Fig. 2) revealed that overall, the organization of the active site inlet in which the condensation reaction takes place is maintained (Fig. 2). Moreover, the architecture of the inlet region is shared between sh*cis*-PT and short- and medium-chain enzymes (*4*, *5*, *35*). Nevertheless, we noticed that R290 of NgBR, a position previously identified as bearing a mutation (R290H) leading to a congenital glycosylation disorder (*22*), switches between two conformations in a substrate-dependent manner. Specifically, R290 only interacts with the substrates when both S_1 and S_2 are occupied (Fig. 2). This conformational switch may support the previously suggested consecutive substrate binding model for *cis*-prenyltransferases in which FPP binding to S_1 precedes the binding of Mg^{2+}-IPP to S_2 (*5*). For the condensation reaction to proceed, Mg^{2+} must transverse between the sites, changing its coordination scheme from involving the pyrophosphate oxygens of IPP to those of the elongating product (Fig. 2). This configuration facilitates the concerted pyrophosphate hydrolysis and nucleophilic attack of the newly formed carbocation at S_1 by the IPP molecule at S_2. Last, a hydrogen is abstracted to neutralize the charge, forming a new *cis* double bond in the product (*5*, *6*). In the crystal structures resolved here, where both sites are occupied before the initiation of pyrophosphate hydrolysis, Mg^{2+} and R290 assume an intermediate position between the sites and interact with the pyrophosphates of both substrates. Thus, by providing charge compensation, it is possible that R290 relieves the Mg^{2+} from S_2, allowing its translocation to S_1.

Our structural analyses further revealed several distinct conformations of the enzyme-product complex (Fig. 3). First, following the condensation and before the binding of an additional IPP molecule (Fig. 3B), the C_{20} product is captured in a bent conformation (at C_{11}), stabilized by hydrophobic interactions with F154 within the hydrophobic pocket. Here, the stopcock N terminus of DHDDS maintains a closed conformation, as observed before the condensation reaction (Figs. 1A and 3A). Next, when an additional substrate molecule occupies S_2, the stopcock switches to an open state, as reflected by the lack of an identifiable electron density for the N terminus of DHDDS (Fig. 3C), forming a new outlet for further product elongation. Curiously, the bent conformation of the product molecule is maintained. This structural plasticity also occurs in solution. This is supported by the high deuterium uptake of the DHDDS N terminus throughout the HDX-MS experiment (Fig. 4). Moreover, the substitution of tryptophan with leucine at position 3 resulted in ~40% increase in the first condensation rate, consistent with the displacement of the N terminus during catalysis (Fig. 6). Last, the product assumes an elongated conformation, protruding through the new outlet (Fig. 3, D to F), keeping the stopcock at an open state, consistent with the limited proteolysis analysis in the absence or presence of substrates (Fig. 3G). This structural organization is in sharp contrast to that previously observed in short- and medium-chain *cis*-prenyltransferases, where the hydrophobic pocket is tightly sealed by a rigid layer of bulky and hydrophobic residues (*35*). In addition, in these enzymes, α3 is shorter and assumes a straight rather than a bent conformation, resulting in a rigid and narrow hydrophobic pocket (*5*, *6*, *9*). These structural differences preclude the opening of an outlet corresponding to that observed in sh*cis*-PT, limiting the product length to the active site dimensions.

In cells, the h*cis*-PT complex is an ER-resident enzyme, anchored to the membrane via the N terminus of NgBR (*15*). In addition, the presence of hydrophobic environment was shown to markedly stimulate enzymatic activity. However, this stimulation is abolished by mutations in hydrophobic residues located at the amphipathic αN of DHDDS, suggesting that interaction with the membrane is crucial for long-chain isoprenoid synthesis (*13*). Combined, these properties align with the proposal that the N terminus of DHDDS can change its conformation to open the active site outlet, allowing direct product elongation into the adjacent membrane bilayer. By monitoring the FRET signal between the fluorescent substrate (Fig. 5) and nanodiscs (Fig. 7), we observed the close proximity of the enzymatic product and the membrane bilayer (Fig. 7D). Moreover, the presence of membranes not only increases catalytic activity but also favors the formation of longer products (Fig. 7B). Last, the time course of chain elongation and emergence of the FRET signal were closely correlated (Fig. 7E). The direct extension of the elongating product, resembling the passing of a thread through the eye of a needle, into the adjacent bilayer, solves two problems. First, as described above, it dismantles the relationship between product length and active site volume, keeping a constant portion of the product within the active site throughout the sequential condensations. Second, as product elongation results in its increased hydrophobicity, concomitant elongation and membrane insertion also serve to avoid the energetic barrier associated with hydrophobic product solvation.

Together, our results support a mechanism in which before the initial condensation reaction, the stopcock formed by the N terminus of DHDDS occludes the active site outlet, shielding its hydrophobic interior from the bulk solvent (Fig. 8A). Following the initial condensation, the stopcock opens and the product extends via the newly formed outlet, enabling the product to come in close proximity to the membrane and eventually to insert into it (Fig. 8B). In principle, this mechanism alleviates any limitation on the final product length and can thus support natural rubber synthesis as well. Notably, when expressed in yeast cells, subunits of rubber synthase produce $C_{80–110}$ products rather than the $>C_{10,000}$ natural rubber formed when coupled with rubber particles (*36*). This suggests that long-chain enzymes and rubber synthases share a basic common synthetic mechanism, further modulated and fine-tuned by additional constituents.

A lingering question remains—what is the mechanism determining the final product length, preventing further condensations and leading to product release? In contrast with short- and medium-chain enzymes in which product length is intrinsically determined by active site dimensions, long-chain *cis*-prenyltransferases and rubber synthases exhibit a population of products of varying lengths (Fig. 7B). This can reflect a tug-of-war mechanism, where the probability of product release is positively correlated with chain lengthening due to cumulative product-membrane interactions and its conformation within the lipid bilayer (Fig. 8B). Such a mechanism can account for the reduction in chain length resulting from disease-causing mutations at the pyrophosphate binding region (*22*, *37*), skewing the balance of forces in favor of the membrane, thus resulting in premature product release. Additional membrane properties, such as curvature, lipid composition, and fluidity, may also play a role in product length determination. In conclusion, our hybrid structural studies exposed a novel product outlet allowing direct and directional elongation of long-chain isoprenoids into adjacent membranes, providing a holistic view of h*cis*-PT catalysis and a structural basis for long-chain isoprenoids and natural rubber synthesis.

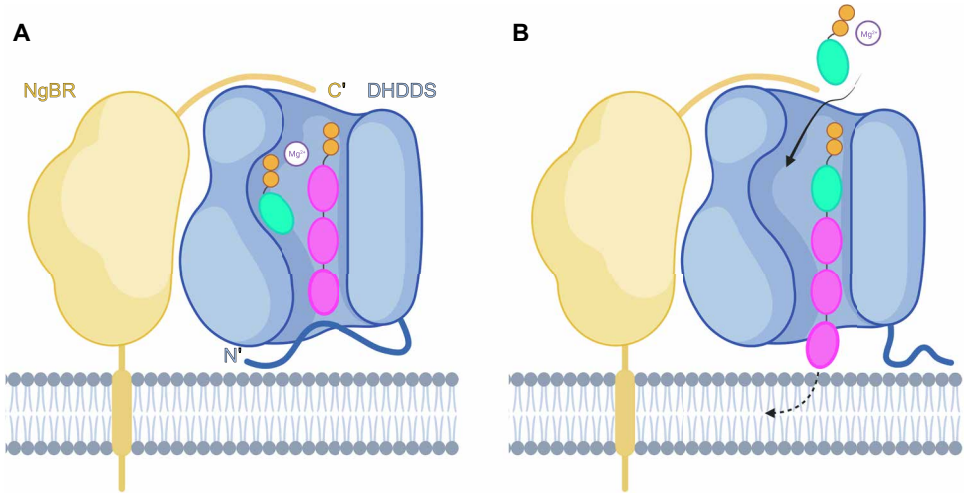

Fig. 8. Proposed model for long-chain isoprenoid synthesis. (**A**) Before the initial condensation reaction, FPP (pink) and IPP (green) occupy the DHDDS active site. The active site outlet is occluded by the DHDDS N terminus. (**B**) Following the condensation reaction, the N terminus of DHDDS dislodges from the outlet, allowing extension of the elongating product to the vicinity of the ER membrane. Further product lengthening is enabled by its insertion into the bilayer. Created with BioRender.com.

MATERIALS AND METHODS

Protein expression and purification

Escherichia coli T7 express competent cells were cotransformed with DHDDS (residues 1 to 333) and NgBR (residues 73 to 293) (sh*cis*-PT) or NgBRΔ167-175 (sh*cis*-PT_{cryst}), grown in Terrific broth medium at 37°C until reaching OD_{600} (optical density at 600 nm) = 0.6 and induced at 16°C by adding 0.5 mM isopropyl β-D-1-thiogalactopyranoside. Proteins were expressed at 16°C for 16 to 20 hours, harvested by centrifugation (~5700*g* for 15 min), and then resuspended in a buffer containing 20 mM Hepes (pH 7.5), 150 mM NaCl, 1 mM tris(2-carboxyethyl)phosphine (TCEP), and 0.02% (w/v) Triton X-100, supplemented with deoxyribonuclease I (1 μg/ml) and a protease inhibitor mixture. Resuspended cells were homogenized and disrupted in a microfluidizer. Soluble proteins were recovered by centrifugation at ~40,000*g* for 45 min at 4°C. Overexpressed proteins were purified on a HisTrap HP column, followed by purification on a Strep-Tactin column and tobacco etch virus (TEV) protease cleavage of the purification tags and thioredoxin fusions. The reaction mixture was concentrated and loaded onto a Superdex-200 preparative size exclusion column preequilibrated with 20 mM Hepes (pH 7.5), 150 mM NaCl, and TCEP. Purified proteins were flash-frozen in liquid nitrogen and stored at −80°C until use. Protein purity was >95%, as judged by SDS–polyacrylamide gel electrophoresis (SDS-PAGE).

Crystallization and data collection

All crystallization trials were performed at 19°C using the sitting drop vapor diffusion method. The sh*cis*-PT_{cryst}–FsPP–IPP complex was crystallized by mixing a protein solution at ~16 mg/ml in the presence of 0.5 mM $MgCl_2$, 0.75 mM FsPP, and 1.5 mM IPP with 0.1 M NaCl, 0.1 M MES (pH 6.5), and 33% (w/v) polyethylene glycol 400 (PEG 400). Data were collected at 100 K using a wavelength of 0.976 Å at the Diamond Light Source (Oxfordshire, UK) beamline I03 (https://doi.org/10.2210/pdb7PAX/pdb). The sh*cis*-PT_{cryst}–GGsPP complex was crystallized by mixing a protein solution at ~14 mg/ml in the presence of 0.5 mM $MgCl_2$, 1 mM FPP, and 2 mM IsPP with 1 M $LiSO_4$, 0.02 M tris-HCl (pH 8.5), and 1.8% (w/v) PEG 8000. Crystals were cryoprotected with 20% glycerol, and data were collected at 100 K using wavelength of 1.000 Å at the European Synchrotron Radiation Facility (ESRF) (Grenoble, France) beamline ID-30B (https://doi.org/10.2210/pdb7PAY/pdb). The sh*cis*-PT_{cryst}–GGsPP–IsPP complex was crystallized by mixing a protein solution at ~12 mg/ml in the presence of 0.5 mM $MgCl_2$, 1 mM FPP, and 2 mM IsPP with 0.1 M KCl, 0.1 M MES (pH 6.5), and 36% (w/v) PEG 400. Data were collected at 100 K using a wavelength of 1.000 Å at the ESRF beamline ID-30B (https://doi.org/10.2210/pdb7PB0/pdb). The sh*cis*-PT_{cryst}–GGPP–IsPP complex was crystallized by mixing a protein solution at ~4 mg/ml in the presence of 0.5 mM $MgCl_2$, 1 mM GGPP, and 2 mM IsPP with 0.07 M MES (pH 6.6), 25% (w/v) PEG 400, 1.5 mM $MgCl_2$, and 4.5% (v/v) ethanol. Data were collected at 100 K using a wavelength of 0.976 Å at the ESRF beamline ID-23-1 (https://doi.org/10.2210/pdb7PB1/pdb). Integration, scaling, and merging of the diffraction data were done with the XDS program (*38*). In the case of sh*cis*-PT_{cryst}–GGPP–IsPP, a dataset with low completeness (~75%) at a resolution of 2.6 Å was merged with a complete dataset (99.1%) at a resolution of 3.1 Å using XDSCONV and XSCALE (*38*).

Structure determination and refinement

All the structures were solved by automated molecular replacement using Phaser (*39*) with the structure of sh*cis*-PT_{cryst}–FPP [Protein Data Bank (PDB) 6Z1N] as a search model. Iterative model building and refinement were carried out in Phenix (*40*) with manual adjustments using Coot (*41*). Ramachandran analysis was performed using MolProbity (*42*). Data collection and refinement statistics are presented in Table 1. Structural illustrations were prepared with UCSF Chimera (www.cgl.ucsf.edu/chimera).

Limited proteolysis

Five micrograms of purified sh*cis*-PT in 20 mM tris-HCl (pH 7.5), 150 mM NaCl, 10 mM β-mercaptoethanol, and 0.5 mM $MgCl_2$ was incubated with 1:1000 trypsin (1 hour on ice), 1:1000 elastase (1 hour at room temperature), or 1:500 α-chymotrypsin (2 hours on ice). For cleavage with chymotrypsin, 10 mM $CaCl_2$ was added to the reaction mixture. Reactions were performed in the absence or

presence of 10 μM FPP or GGPP. The reactions were quenched by the addition of sample buffer and thermal denaturation at 90°C for 10 min, followed by SDS-PAGE analysis.

Hydrogen-deuterium exchange mass spectrometry

For peptide identification, sh*cis*-PT was diluted to 2 μM concentration in 20 mM Hepes (pH 7.5), 150 mM NaCl, 1 mM EDTA, and 1 mM TCEP and subsequently mixed with equal volume (50 + 50 μl) of 1 M glycine-HCl (pH 2.3). Mixture was frozen in liquid nitrogen. Before the analysis, the sample was quickly thawed and injected onto an liquid chromatography (LC) system coupled to an electrospray ionization source of 15-T Fourier-transform ion cyclotron resonance (FT-ICR) mass spectrometer (solariX XR, Bruker Daltonics, Germany) operating in data-dependent mode, where each full scan was followed by six tandem mass spectrometry (MS/MS) scans [collision-induced dissociation analyses (CID)] of the top most abundant ions. Repeat count was set to 2, and exclusion was set to 10 parts per million and 30-s duration. Instrument was calibrated externally using sodium trifluoroacetic acid clusters resulting in sub–parts per million mass error. The LC method started by an online digestion on the custom-made pepsin column (bed volume, 66 μl) (*43*). Generated peptides were trapped and desalted on a VanGuard Pre-column (ACQUITY UPLC BEH C18, 130 Å, 1.7 μm, 2.1 mm by 5 mm, Waters, USA). The digestion and desalting (total time, 3 min) were driven by 0.4% formic acid (FA) in water pumped by 1260 Infinity II Quaternary pump (Agilent Technologies, Germany) at a flow rate of 100 μl min^{-1}. Desalted peptides were then separated on an analytical column (ACQUITY UPLC BEH C18, 130 Å, 1.7 μm, 1 mm by 100 mm, Waters, USA) using linear gradient (5 to 45% B in 7 min), followed by a quick step to 99% B lasting 5 min, where the solvent A was 0.1% FA/2% acetonitrile (ACN) in water, and solvent B was 0.1% FA/98% ACN in water. The gradient was delivered by the 1290 Infinity II LC System (Agilent Technologies, Germany) at a flow rate of 40 μl min^{-1}. LC–MS/MS analysis for peptide identification was followed by MASCOT 2.7 database searching against a custom-built database combining crap database, sequence of used acidic protease, and the sequences of sh*cis*-PT subunits. MSTools was used to plot the identified peptides against the protein sequence (*44*).

Backbone amide HDX was initiated by a 10-fold dilution of the protein solution into D_2O-based solution containing 20 mM Hepes (pD 7.5), 150 mM NaCl, 1 mM EDTA, and 1 mM TCEP. The exchange was followed for 20 s, 1 min, 3 min, 10 min, 30 min, 1 hour, and 3 hours at 20°C and quenched by the addition of 0.5 M glycine-HCl (pH 2.3) in a 1:1 ratio and flash freezing in liquid nitrogen. The labeling experiment was done in duplicate. LC-MS analysis of deuterated samples was started by rapid thawing of the sample and injection onto the custom-made pepsin column (bed volume, 66 μl). Following LC, method was identical to that used for peptide identification and mentioned above (*43*). A 15-T FT-ICR mass spectrometer was operating in broadband MS mode. Acquired data were exported using DataAnalysis 5.0, processed by the in-house designed Deutex software and handled as described previously (*45*, *46*). Fully deuterated control was prepared as described previously (*46*), and correction for back-exchange was applied (*32*).

Yeast complementation assay

The *Saccharomyces cerevisiae* strain K405, lacking the yeast DHDDS and NgBR homologs (Δ *nus1*, Δ *rer2*, and Δ *srt1*) and carrying the Gl*cis*-PT on a plasmid bearing the *URA3* selection marker, was used (*22*). To analyze DHDDS N-terminal mutants, cells were transformed using the standard lithium-acetate method with the DHDDS.GW1 (WT or mutants thereof) and NgBR.GW2 plasmids, bearing leucine and methionine selection markers, respectively. Empty vectors were used as negative controls, and Gl-*cis*PT.GW1 was used as a positive control. Following transformation, cells were plated on solid synthetic defined medium lacking uracil, methionine, and leucine and incubated for 48 to 72 hours at 30°C. Next, single colonies were inoculated into liquid synthetic defined medium lacking uracil, methionine, and leucine, incubated overnight at 30°C using a shaker, and diluted to reach OD_{600} = 1. For phenotypic analysis, 10-fold serial dilutions were performed, and transformants were spotted on solid synthetic defined complete medium supplemented with 0.1% (w/v) 5-fluoroorotic acid (FOA) plates and incubated at 30°C for 5 days. Synthetic defined medium was made of 0.67% (w/v) yeast nitrogen base and 2% (w/v) supplemented with auxotrophic requirements. For solid medium, agar was added at a 2% (w/v) final concentration.

Enzyme kinetics

The activity of purified sh*cis*-PT was measured using a radioligand-based assay (*12*, *26*, *47*, *48*). Purified sh*cis*-PT (0.1 μM) was mixed with [^{14}C]-IPP and MANT-O-GPP or FPP to initiate the reaction in buffer composed of 25 mM tris-HCl (pH 7.5), 150 mM NaCl, 10 mM β-mercaptoethanol, 0.02% (v/v) Triton X-100, and 0.5 mM $MgCl_2$ at 30°C. EDTA (15 mM; final concentration) was added to quench the reaction, and 500 μl of water-saturated 1-butanol was added to extract the reaction products by thorough vortexing. Initial rates were measured by quenching the reaction at 10% or lower substrate consumption. The products, encompassing ^{14}C, were quantitated using a scintillation counter. The K_m values of MANT-O-GPP or FPP were determined by varying their concentrations while holding [IPP] constant at 100 μM. Kinetic constants were obtained by fitting the data to the Michaelis-Menten equation using Origin 7.0.

Fluorescence spectroscopy

MANT-O-GPP was synthesized as previously described. All fluorescence experiments were performed in triplicate using a RF-8500 spectrofluorometer (Jasco, Japan) in fluorescence buffer [20 mM tris-HCl (pH 7.5), 150 mM NaCl, 10 mM β-mercaptoethanol, and 0.5 mM $MgCl_2$]. FRET experiments between sh*cis*-PT and MANT-O-GPP were performed using 1 μM purified sh*cis*-PT (WT or W3L) preincubated with 0 to 16 μM MANT-O-GPP. The competition with FPP was performed by preincubation with varying [FPP] (0 to 100 μM) while holding [MANT-O-GPP] constant at 10 μM. To obtain the dose-response curves, the F_{420}/F_{340} ratio was calculated for each fluorescence spectrum, and the F_{420}/F_{340} ratio of the apo protein was subtracted. The activity of sh*cis*-PT in the presence of azolectin nanodiscs was measured by using 0.1 μM purified sh*cis*-PT preincubated with the indicated ratio of nanodiscs in the presence of 2 μM MANT-O-GPP and 40 μM IPP. Experiments with fluorescent nanodiscs were carried out under the same conditions using a constant concentration of 0.2 μM nanodiscs. Data were fit using Prism GraphPad 9.0.1.

Stopped-flow kinetics

Experiments were performed using the RF-8500 spectrofluorometer SFS-852 stopped-flow module (Jasco, Japan). Fifty microliters of 2 μM sh*cis*-PT (WT or W3L) preincubated with 2 μM MANT-O-GPP in

fluorescence buffer was mixed with 50 µl of 10 µM IsPP in fluorescence buffer at 10 ml/s, resulting in a dead time of ~4 ms. Fluorescence intensity at 420 nm was measured following excitation at 280 nm. Data were fit to a one-phase exponential equation with Bio-Kine 32 V4.45.

Thin-layer chromatography

Products were obtained by incubating 1 µM purified sh*cis*-PT with 25 µM MANT-O-GPP and 500 µM IPP in a buffer composed of 50 mM Hepes (pH 7.5), 150 mM NaCl, 10 mM β-mercaptoethanol, and 1 mM $MgCl_2$ at 30°C, with or without 2 µM nanodiscs, for 4 hours. Water-saturated 1-butanol was added to extract the reaction products by thorough vortexing, followed by centrifugation at 21,000*g* for 10 min for phase separation. The organic phase was transferred to a glass vial and evaporated under a mild nitrogen stream. Next, the products of each reaction were dephosphorylated by adding 1 ml of 50 mM sodium acetate/acetic acid (pH 4.7), 20% (v/v) isopropanol, and 0.1% (v/v) Triton X-100, supplemented with 4.4 U of potato acidic phosphatase (*49*). Following overnight incubation at 37°C, dephosphorylated products were extracted with *n*-hexane by thorough vortexing, followed by centrifugation at 21,000*g* for 10 min for phase separation. The organic phase was transferred to a glass vial, evaporated under a mild nitrogen stream, and resuspended in 100 µl of methanol. The dephosphorylated products were loaded onto a high-performance thin-layer chromatography (HPTLC) silica gel 60 RP-18 plate with a concentrating zone, run in acetone:50 mM H_3PO_4 mixture (39:1), and visualized under ultraviolet illumination (λ = 365 nm). MANT-O-geraniol was used as an internal standard.

Nanodisc preparation

Membrane scaffold protein 1E3D1 (MSP1E3D1) was overexpressed and purified as previously described (*50*). Briefly, hexahistidine-tagged MSP1E3D1 was overexpressed in *E. coli* and purified using immobilized metal affinity chromatography, followed by tag cleavage with TEV protease and size exclusion chromatography in nanodisc buffer [20 mM Hepes (pH 7.5) and 150 mM NaCl]. Nanodiscs were prepared by mixing 0.2 mM MSP1E3D1 in nanodisc buffer supplemented with 10 mM azolectin in the presence or absence of 1% (mol/mol) PE-NBD in 50 mM cholate. Nanodisc buffer was added to achieve a final cholate concentration of 20 mM, and the nanodisc assembly mixture was incubated for 1 hour at room temperature. Next, biobeads (1 mg/ml) were added in two steps, where half of the biobeads were incubated for 1 hour and the other were incubated for 3 hours at room temperature. Last, the reaction volume was centrifuged for 5 min at 21,000*g* and loaded onto a Superdex-200 preparative size exclusion column prewashed with nanodisc buffer.

SUPPLEMENTARY MATERIALS

Supplementary material for this article is available at https://science.org/doi/10.1126/sciadv.abn1171

View/request a protocol for this paper from *Bio-protocol*.

REFERENCES AND NOTES

1. S. A. Holstein, R. J. Hohl, Isoprenoids: Remarkable diversity of form and function. *Lipids* **39**, 293–309 (2004).
2. J. C. Sacchettini, C. D. Poulter, Creating isoprenoid diversity. *Science* **277**, 1788–1789 (1997).
3. K. Ogura, T. Koyama, Enzymatic aspects of isoprenoid chain elongation. *Chem. Rev.* **98**, 1263–1276 (1998).
4. P. H. Liang, T. P. Ko, A. H. J. Wang, Structure, mechanism and function of prenyltransferases. *Eur. J. Biochem.* **269**, 3339–3354 (2002).
5. C. C. Chen, L. Zhang, X. Yu, L. Ma, T. P. Ko, R. T. Guo, Versatile *cis*-isoprenyl diphosphate synthase superfamily members in catalyzing carbon–carbon bond formation. *ACS Catal.* **10**, 4717–4725 (2020).
6. S. Yamashita, S. Takahashi, Molecular mechanisms of natural rubber biosynthesis. *Annu. Rev. Biochem.* **89**, 821–851 (2020).
7. K. A. Grabińska, E. J. Park, W. C. Sessa, *Cis*-prenyltransferase: New insights into protein glycosylation, rubber synthesis, and human diseases. *J. Biol. Chem.* **291**, 18582–18590 (2016).
8. P. H. Liang, Reaction kinetics, catalytic mechanisms, conformational changes, and inhibitor design for prenyltransferases. *Biochemistry* **48**, 6562–6570 (2009).
9. Y. Kharel, S. Takahashi, S. Yamashita, T. Koyama, Manipulation of prenyl chain length determination mechanism of *cis*-prenyltransferases. *FEBS J.* **273**, 647–657 (2006).
10. S. Takahashi, T. Koyama, Structure and function of *cis*-prenyl chain elongating enzymes. *Chem. Rec.* **6**, 194–205 (2006).
11. M. Noike, T. Ambo, S. Kikuchi, T. Suzuki, S. Yamashita, S. Takahashi, H. Kurokawa, S. Mahapatra, D. C. Crick, T. Koyama, Product chain-length determination mechanism of *Z,E*-farnesyl diphosphate synthase. *Biochem. Biophys. Res. Commun.* **377**, 17–22 (2008).
12. M. L. Bar-El, P. Vaňková, A. Yeheskel, L. Simhaev, H. Engel, P. Man, Y. Haitin, M. Giladi, Structural basis of heterotetrameric assembly and disease mutations in the human *cis*-prenyltransferase complex. *Nat. Commun.* **11**, 5273 (2020).
13. B. H. Edani, K. A. Grabinska, R. Zhang, E. J. Park, B. Siciliano, L. Surmacz, Y. Ha, W. C. Sessa, Structural elucidation of the *cis*-prenyltransferase NgBR/DHDDS complex reveals insights in regulation of protein glycosylation. *Proc. Natl. Acad. Sci. U.S.A.* **117**, 20794–20802 (2020).
14. M. Welti, Regulation of dolichol-linked glycosylation. *Glycoconj. J.* **30**, 51–56 (2013).
15. K. D. Harrison, E. J. Park, N. Gao, A. Kuo, J. S. Rush, C. J. Waechter, M. A. Lehrman, W. C. Sessa, Nogo-B receptor is necessary for cellular dolichol biosynthesis and protein N-glycosylation. *EMBO J.* **30**, 2490–2500 (2011).
16. L. Zelinger, E. Banin, A. Obolensky, L. Mizrahi-Meissonnier, A. Beryozkin, D. Bandah-Rozenfeld, S. Frenkel, T. Ben-Yosef, S. Merin, S. B. Schwartz, A. V. Cideciyan, S. G. Jacobson, D. Sharon, A missense mutation in DHDDS, encoding dehydrodolichyl diphosphate synthase, is associated with autosomal-recessive retinitis pigmentosa in Ashkenazi Jews. *Am. J. Hum. Genet.* **88**, 207–215 (2011).
17. B. L. Lam, S. L. Züchner, J. Dallman, R. Wen, E. C. Alfonso, J. M. Vance, M. A. Peričak-Vance, Mutation K42E in dehydrodolichol diphosphate synthase (DHDDS) causes recessive retinitis pigmentosa. *Adv. Exp. Med. Biol.* **801**, 165–170 (2014).
18. F. F. Hamdan, C. T. Myers, P. Cossette, P. Lemay, D. Spiegelman, A. D. Laporte, C. Nassif, O. Diallo, J. Monlong, M. Cadieux-Dion, S. Dobrzeniecka, C. Meloche, K. Retterer, M. T. Cho, J. A. Rosenfeld, W. Bi, C. Massicotte, M. Miguet, L. Brunga, B. M. Regan, K. Mo, C. Tam, A. Schneider, G. Hollingsworth; Deciphering Developmental Disorders Study, D. R. FitzPatrick, A. Donaldson, N. Canham, E. Blair, B. Kerr, A. E. Fry, R. H. Thomas, J. Shelagh, J. A. Hurst, H. Brittain, M. Blyth, R. R. Lebel, E. H. Gerkes, L. Davis-Keppen, Q. Stein, W. K. Chung, S. J. Dorison, P. J. Benke, E. Fassi, N. Corsten-Janssen, E. J. Kamsteeg, F. T. Mau-Them, A. L. Bruel, A. Verloes, K. Õunap, M. H. Wojcik, D. V. F. Albert, S. Venkateswaran, T. Ware, D. Jones, Y. C. Liu, S. S. Mohammad, P. Bizargity, C. A. Bacino, V. Leuzzi, S. Martinelli, B. Dallapiccola, M. Tartaglia, L. Blumkin, K. J. Wierenga, G. Purcarin, J. J. O'Byrne, S. Stockler, A. Lehman, B. Keren, M. C. Nougues, C. Mignot, S. Auvin, C. Nava, S. M. Hiatt, M. Bebin, Y. Shao, F. Scaglia, S. R. Lalani, R. E. Frye, I. T. Jarjour, S. Jacques, R. M. Boucher, E. Riou, M. Srour, L. Carmant, A. Lortie, P. Major, P. Diadori, F. Dubeau, G. D'Anjou, G. Bourque, S. F. Berkovic, L. G. Sadleir, P. M. Campeau, Z. Kibar, R. G. Lafrenière, S. L. Girard, S. Mercimek-Mahmutoglu, C. Boelman, G. A. Rouleau, I. E. Scheffer, H. C. Mefford, D. M. Andrade, E. Rossignol, B. A. Minassian, J. L. Michaud, High rate of recurrent de novo mutations in developmental and epileptic encephalopathies. *Am. J. Hum. Genet.* **101**, 664–685 (2017).
19. G. Piccolo, E. Amadori, M. S. Vari, F. Marchese, A. Riva, V. Ghirotto, M. Iacomino, V. Salpietro, F. Zara, P. Striano, Complex neurological phenotype associated with a de novo *DHDDS* mutation in a boy with intellectual disability, refractory epilepsy, and movement disorder. *J. Pediatr. Genet.* **10**, 236–238 (2021).
20. S. Galosi, B. H. Edani, S. Martinelli, H. Hansikova, E. A. Eklund, C. Caputi, L. Masuelli, N. Corsten-Janssen, M. Srour, R. Oegema, D. G. M. Bosch, C. A. Ellis, L. Amlie-Wolf, A. Accogli, I. Atallah, L. Averdunk, K. W. Barañano, R. Bei, I. Bagnasco, A. Brusco, S. Demarest, A.-S. Alaix, C. Di Bonaventura, F. Distelmaier, F. Elmslie, Z. Gan-Or, J.-M. Good, K. Gripp, E.-J. Kamsteeg, E. Macnamara, C. Marcelis, N. Mercier, J. Peeden, S. Pizzi, L. Pannone, M. Shinawi, C. Toro, N. E. Verbeek, S. Venkateswaran, P. G. Wheeler, L. Zdrazilova, R. Zhang, G. Zorzi, R. Guerrini, W. C. Sessa, D. Lefeber, M. Tartaglia, F. F. Hamdan, K. A. Grabińska, V. Leuzzi, De novo DHDDS variants cause a neurodevelopmental and neurodegenerative disorder with myoclonus. *Brain* **145**, 208–223 (2021).
21. C. Courage, K. L. Oliver, E. J. Park, J. M. Cameron, K. A. Grabińska, M. Muona, L. Canafoglia, A. Gambardella, E. Said, Z. Afawi, B. Baykan, C. Brandt, C. di Bonaventura, H. B. Chew, C. Criscuolo, L. M. Dibbens, B. Castellotti, P. Riguzzi, A. Labate, A. Filla, A. T. Giallonardo,

G. Berecki, C. B. Jackson, T. Joensuu, J. A. Damiano, S. Kivity, A. Korczyn, A. Palotie, P. Striano, D. Uccellini, L. Giuliano, E. Andermann, I. E. Scheffer, R. Michelucci, M. Bahlo, S. Franceschetti, W. C. Sessa, S. F. Berkovic, A. E. Lehesjoki, Progressive myoclonus epilepsies—Residual unsolved cases have marked genetic heterogeneity including dolichol-dependent protein glycosylation pathway genes. *Am. J. Hum. Genet.* **108**, 722–738 (2021).
22. E. J. Park, K. A. Grabińska, Z. Guan, V. Stránecký, H. Hartmannová, K. Hodaňová, V. Barešová, J. Sovová, L. Jozsef, N. Ondrušková, H. Hansíková, T. Honzík, J. Zeman, H. Hůlková, R. Wen, S. Kmoch, W. C. Sessa, Mutation of Nogo-B receptor, a subunit of *cis*-prenyltransferase, causes a congenital disorder of glycosylation. *Cell Metab.* **20**, 448–457 (2014).
23. S. Sabry, S. Vuillaumier-Barrot, E. Mintet, M. Fasseu, V. Valayannopoulos, D. Héron, N. Dorison, C. Mignot, N. Seta, I. Chantret, T. Dupré, S. E. H. Moore, A case of fatal type I congenital disorders of glycosylation (CDG I) associated with low dehydrodolichol diphosphate synthase (DHDDS) activity. *Orphanet J. Rare Dis.* **11**, 1–14 (2016).
24. F. Schwarz, M. Aebi, Mechanisms and principles of N-linked protein glycosylation. *Curr. Opin. Struct. Biol.* **21**, 576–582 (2011).
25. J. Ma, T.-P. Ko, X. Yu, L. Zhang, L. Ma, C. Zhai, R.-T. Guo, W. Liu, H. Li, C.-C. Chen, Structural insights to heterodimeric *cis*-prenyltransferases through yeast dehydrodolichyl diphosphate synthase subunit Nus1. *Biochem. Biophys. Res. Commun.* **515**, 621–626 (2019).
26. M. L. Bar-El, S. Y. Lee, A. Y. Ki, N. Kapelushnik, A. Loewenstein, K. Y. Chung, D. Schneidman-Duhovny, M. Giladi, H. Newman, Y. Haitin, Structural characterization of full-length human dehydrodolichyl diphosphate synthase using an integrative computational and experimental approach. *Biomolecules* **9**, 660 (2019).
27. T. P. Ko, Y. K. Chen, H. Robinson, P. C. Tsai, Y. G. Gao, A. P. C. Chen, A. H. J. Wang, P. H. Liang, Mechanism of product chain length determination and the role of a flexible loop in *Escherichia coli* undecaprenyl-pyrophosphate synthase catalysis. *J. Biol. Chem.* **276**, 47474–47482 (2001).
28. K. A. Grabińska, B. H. Edani, E. J. Park, J. R. Kraehling, W. C. Sessa, A conserved C-terminal RXG motif in the NgBR subunit of *cis*-prenyltransferase is critical for prenyltransferase activity. *J. Biol. Chem.* **292**, 17351–17361 (2017).
29. Y. H. Chen, A. P. C. Chen, C. T. Chen, A. H. J. Wang, P. H. Liang, Probing the conformational change of *Escherichia coli* undecaprenyl pyrophosphate synthase during catalysis using an inhibitor and tryptophan mutants. *J. Biol. Chem.* **277**, 7369–7376 (2002).
30. R. M. Phan, C. Dale Poulter, Synthesis of (*S*)-isoprenoid thiodiphosphates as substrates and inhibitors. *J. Org. Chem.* **66**, 6705–6710 (2001).
31. X. Yan, C. S. Maier, Hydrogen/deuterium exchange mass spectrometry. *Methods Mol. Biol.* **492**, 255–271 (2009).
32. Z. Zhang, D. L. Smith, Determination of amide hydrogen exchange by mass spectrometry: A new tool for protein structure elucidation. *Protein Sci.* **2**, 522–531 (1993).
33. K. H. Teng, A. P. C. Chen, C. J. Kuo, Y. C. Li, H. G. Liu, C. T. Chen, P. H. Liang, Fluorescent substrate analog for monitoring chain elongation by undecaprenyl pyrophosphate synthase in real time. *Anal. Biochem.* **417**, 136–141 (2011).
34. P. Wu, L. Brand, Resonance energy transfer: Methods and applications. *Anal. Biochem.* **218**, 1–13 (1994).
35. S. Y. Chang, T. P. Ko, P. H. Liang, A. H. J. Wang, Catalytic mechanism revealed by the crystal structure of undecaprenyl pyrophosphate synthase in complex with sulfate, magnesium, and Triton. *J. Biol. Chem.* **278**, 29298–29307 (2003).
36. S. Takahashi, H.-J. Lee, S. Yamashita, T. Koyama, Characterization of *cis*-prenyltransferases from the rubber producing plant *Hevea brasiliensis* heterologously expressed in yeast and plant cells. *Plant Biotechnol.* **29**, 411–417 (2012).
37. R. Wen, B. L. Lam, Z. Guan, Aberrant dolichol chain lengths as biomarkers for retinitis pigmentosa caused by impaired dolichol biosynthesis. *J. Lipid Res.* **54**, 3516–3522 (2013).
38. W. Kabsch, XDS. *Acta Crystallogr. Sect. D Biol. Crystallogr.* **66**, 125–132 (2010).
39. A. J. McCoy, R. W. Grosse-Kunstleve, P. D. Adams, M. D. Winn, L. C. Storoni, R. J. Read, Phaser crystallographic software. *J. Appl. Cryst.* **40**, 658–674 (2007).
40. P. D. Adams, P. V. Afonine, G. Bunkóczi, V. B. Chen, I. W. Davis, N. Echols, J. J. Headd, L. W. Hung, G. J. Kapral, R. W. Grosse-Kunstleve, A. J. McCoy, N. W. Moriarty, R. Oeffner, R. J. Read, D. C. Richardson, J. S. Richardson, T. C. Terwilliger, P. H. Zwart, PHENIX: A comprehensive Python-based system for macromolecular structure solution. *Acta Crystallogr. Sect. D Biol. Crystallogr.* **66**, 213–221 (2010).
41. P. Emsley, K. Cowtan, Coot: Model-building tools for molecular graphics. *Acta Crystallogr. Sect. D Biol. Crystallogr.* **60**, 2126–2132 (2004).
42. V. B. Chen, W. B. Arendall III, J. J. Headd, D. A. Keedy, R. M. Immormino, G. J. Kapral, L. W. Murray, J. S. Richardson, D. C. Richardson, *MolProbity*: All-atom structure validation for macromolecular crystallography. *Acta Crystallogr. Sect. D Biol. Crystallogr.* **66**, 12–21 (2010).
43. A. Kadek, H. Mrazek, P. Halada, M. Rey, D. C. Schriemer, P. Man, Aspartic protease nepenthesin-1 as a tool for digestion in hydrogen/deuterium exchange mass spectrometry. *Anal. Chem.* **86**, 4287–4294 (2014).
44. D. Kavan, P. Man, MSTools—Web-based application for visualization and presentation of HXMS data. *Int. J. Mass Spectrom.* **302**, 53–58 (2011).
45. F. Trcka, M. Durech, P. Vankova, J. Chmelik, V. Martinkova, J. Hausner, A. Kadek, J. Marcoux, T. Klumpler, B. Vojtesek, P. Muller, P. Man, Human stress-inducible Hsp70 has a high propensity to form ATP-dependent antiparallel dimers that are differentially regulated by cochaperone binding. *Mol. Cell. Proteomics* **18**, 320–337 (2019).
46. P. Vankova, E. Salido, D. J. Timson, P. Man, A. L. Pey, A dynamic core in human NQO1 controls the functional and stability effects of ligand binding and their communication across the enzyme dimer. *Biomolecules* **9**, 728 (2019).
47. M. Giladi, I. Edri, M. Goldenberg, H. Newman, R. Strulovich, D. Khananshvili, Y. Haitin, A. Loewenstein, Purification and characterization of human dehydrodolychil diphosphate synthase (DHDDS) overexpressed in *E. coli*. *Protein Expr. Purif.* **132**, 138–142 (2017).
48. I. Edri, M. Goldenberg, M. Lisnyansky, R. Strulovich, H. Newman, A. Loewenstein, D. Khananshvili, M. Gilad, Y. Haitin, Overexpression and purification of human *cis*-prenyltransferase in *Escherichia coli*. *J. Vis. Exp.* **2017**, 56430 (2017).
49. H. Fujii, T. Koyama, K. Ogura, Efficient enzymatic hydrolysis of polyprenyl pyrophosphates. *Biochim. Biophys. Acta* **712**, 716–718 (1982).
50. F. Hagn, M. L. Nasr, G. Wagner, Assembly of phospholipid nanodiscs of controlled size for structural studies of membrane proteins by NMR. *Nat. Protoc.* **13**, 79–98 (2018).

Acknowledgments: We acknowledge the ESRF for provision of synchrotron radiation facilities, and we would like to thank M. Soler-López and C. Mueller-Dieckmann for assistance in using beamlines ID-23-1 and ID-30B, respectively. We also acknowledge the Diamond Light Source for provision of synchrotron radiation facilities, and we would like to thank F. Bertram for assistance in using beamline I03. The KG405 yeast strain and DHDDS.GW1 and NgBR.GW2 expression vectors were provided by W. C. Sessa. **Funding:** This work was supported by the Israel Science Foundation grant 1721/16 (to Y.H.); Israel Science Foundation grant 1653/21 (to Y.H.); Israel Cancer Research Fund grant 01214 (to Y.H.); Israel Cancer Research Fund grant 19202 (to M.G.); Israel Cancer Association grant 20200037 (to M.G. and Y.H.); German-Israeli Foundation for Scientific Research and Development grant I-2425-418.13/2016 (to Y.H.); I-CORE Program of the Planning and Budgeting Committee and The Israel Science Foundation grant 1775/12 (to Y.H.); Kahn foundation's Orion project, Tel Aviv Medical Center, Israel (to M.G.); Claire and Amedee Maratier Institute for the Study of Blindness and Visual Disorders, Sackler Faculty of Medicine, Tel-Aviv University (to Y.H. and M.G.); EU Horizon 2020 grant EU_FT–ICR_MS project number 731077 (to P.M.); CIISB grant LM2018127 (to P.M.); and MEYS CZ grant CZ.1.05/1.1.00/02.0109 (to P.M. and P.V.). **Author contributions:** Conceptualization: M.G. and Y.H. Methodology: M.G., P.M., and Y.H. Investigation: M.G., M.L.B.-E., P.V., A.F., E.M., S.A., B.R., E.H., R.W., D.K., P.M., and Y.H. Visualization: D.K. Supervision: M.G. and Y.H. Writing—original draft: M.G. and Y.H. Writing—review and editing: M.G., P.M., R.W., and Y.H. **Competing interests:** The authors declare that they have no competing interests. **Data and materials availability:** Atomic coordinates and structure factors for the structures of sh*cis*-PT_{cryst} have been deposited in the PDB under accession codes 7PAX (in complex with Mg^{2+}, FsPP, and IPP), 7PAY (in complex with Mg^{2+} and GGsPP), 7 PB0 (in complex with Mg^{2+}, GGsPP, and IsPP), and 7 PB1 (in complex with Mg^{2+}, GGPP, and IsPP). The MS proteomics data have been deposited to the ProteomeXchange Consortium via the PRIDE partner repository with the dataset identifier PXD031707. All other data are available in the main text or the Supplementary Materials (figs. S1 to S3).

Submitted 5 November 2021
Accepted 1 April 2022
Published 18 May 2022
10.1126/sciadv.abn1171